J. Wind Eng. Ind. Aerodyn. 147 (2015) 95–103

Contents lists available at ScienceDirect

Journal of Wind Engineering and Industrial Aerodynamics

journal homepage: www.elsevier.com/locate/jweia

Effect of aspect ratio on the near-wake flow structure of an Ahmed body

M. Corallo, J. Sheridan, M.C. Thompson

Department of Mechanical and Aerospace Engineering, Monash University, Clayton, Victoria 3800, Australia

ARTICLE INFO

Article history:
Received 23 January 2015
Received in revised form
10 September 2015
Accepted 16 September 2015

Keywords:
Ahmed body
Aspect ratio
C-Pillar vortex

ABSTRACT

Through numerical simulations, the interaction between the longitudinal c-pillar vortices and the flow over the rear slant surface is established for an *Ahmed-body* geometry as its aspect ratio is varied. In turn this affects the flow structure and topology of the near wake, and has a significant effect on the drag.

In particular, aspect ratio was found to influence the critical angle at which flow fully separates on the rear slant surface due to the interaction of the c-pillar vortices with the rear slant flow. This appears to be a consequence of the influence that downwash generated by the c-pillar vortices has on promoting rear slant flow reattachment. By isolating the pressure drag associated with individual surfaces, it is shown that the drag discontinuity is almost entirely due to a sudden change in the pressure field on the rear slant surface. On increasing the aspect ratio, once the flow becomes fully separated, c-pillar vortex strength and position change considerably, inferring a mutual relationship between flow reattachment and c-pillar vortex generation mechanisms for the Ahmed-body geometry.

1. Introduction

The aerodynamic forces experienced by a body are directly affected by its wake structure. To make this point explicit, several methods exist to evaluate the force components from velocity field data on a control-volume surface enclosing the body (e.g., Noca et al., 1999; Tan et al., 2005), inferring that a change in wake structure will have a direct influence on the forces experienced by the body. Furthermore, the individual contributions of identifiable flow structures to the overall force can be quantified (Onorato et al., 1984; Roshko, 1954).

The dominant wake structures of a body are highly dependent on geometry. Spanwise vortex structures, such as Kármán vortices, are commonly observed for quasi-two-dimensional bodies, such as high aspect-ratio circular and rectangular cylinders (Okajima et al., 1992; Williamson, 1996). Three-dimensional bodies often exhibit more complex wake structures comprised of coexisting streamwise and spanwise vortices (Baker, 2010; Gilhome et al., 2001; Payne et al., 1986). An important component of three-dimensionality of the wake in the case of three-dimensional bodies is due to the influence of the end boundaries on the vortex shedding mechanism (Gerich and Eckelmann, 1982).

The forces on different automotive geometries vary considerably. This is often the result of large changes in wake structure caused by geometrical differences, though detailed shape optimisation also plays a key role in overall body forces (Janssen and Hucho, 1975). In the case of the hatchback vehicle, identical critical wake flow behaviour can be generated though the use of simplified models (Morel, 1978). These simplified reference models allow fundamental aerodynamic characteristics to be analysed without the added complexity caused by detailed body shape (Good and Garry, 2004).

Of the numerous simplified automotive reference models available, the Ahmed body (Ahmed et al., 1984) is one of the most widely adopted in research undertaken to study the effect of constrained geometry changes on aerodynamic flow fields and loading. The Ahmed body is a simplified hatchback automotive model that exhibits the characteristic critical wake flow behaviour of hatchbacks first observed by Janssen and Hucho (1975), while its simplified geometry aims to achieve separation-free flow over the front of the model and relatively uniform flow through the middle section. The Ahmed body drag curve (Fig. 1) demonstrates the discontinuous change associated with a change in flow regime as the slant angle (θ) is varied; a phenomenon characteristic of hatchback vehicles.

The Ahmed body wake flow structure under high drag conditions ($\theta < 30^{\circ}$, see Fig. 2) is dominated by a large pair of counter-rotating vortices emanating from the c-pillars of the model (F in Fig. 2) (Ahmed et al., 1984; Lienhart et al., 2002). Flow over the slant surface detaches at its leading edge and reattaches further downstream (E), while at the base of the model there are two recirculating flow regions situated one above the other. It has been suggested that the c-pillar vortices play a strong role in promoting

E-mail address: matt.corallo@gmail.com (M. Corallo).

http://dx.doi.org/10.1016/j.jweia.2015.09.006
0167-6105/

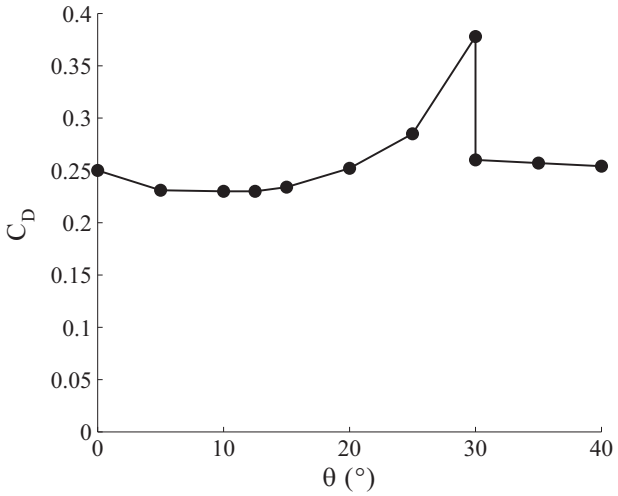

Fig. 1. Characteristic Ahmed-body drag profile (Ahmed et al., 1984).

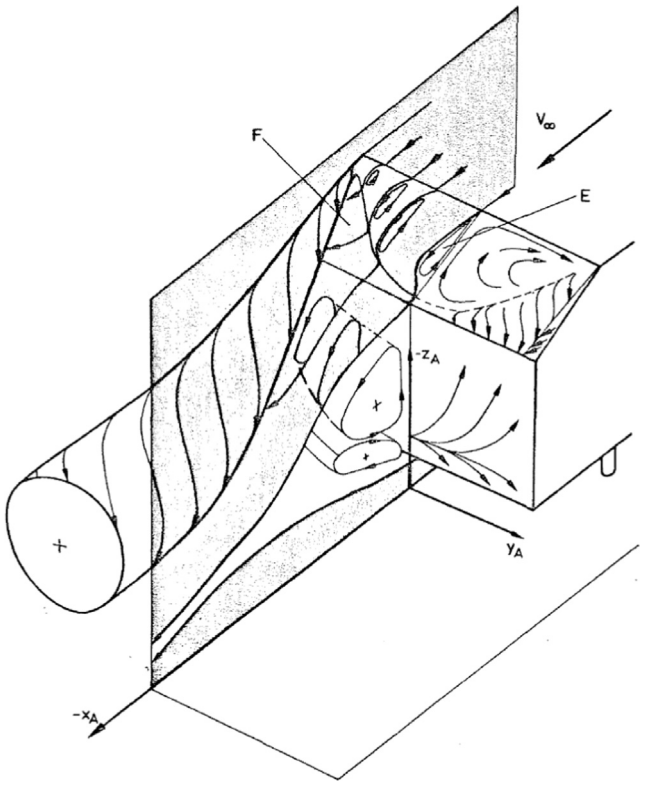

Fig. 2. Characteristic Ahmed-body wake flow for high-drag flow regime (Ahmed et al., 1984). Reprinted with permission from SAE paper 840300 © 1984 SAE International.

flow reattachment over the slant surface of the model (Hucho and Sovran, 1993; Wang et al., 2013), due to the associated downwash onto the slant surface.

Early work by Morel (1978) touched on the influence of c-pillar vortices on flow reattachment. A difference in critical slant angle of 12° was observed between an axisymmetric cylinder with a slanted base and a simplified automotive hatchback model. The shift was attributed to a change in aspect ratio of the slant surface, resulting in a decrease in the influence of the c-pillar vortices on the overall flow over the slant and a breakdown of attached flow at a lower slant angle.

This paper investigates the effect that aspect ratio has on the interaction of c-pillar vortex structures in the wake of an Ahmed model. It is anticipated that this will lead to new insight on the influence that c-pillar vortices have on promoting flow reattachment on the rear slant of the model at high slant angles.

2. Numerical methodology

The geometry used was the simplified automotive hatchback model introduced by Ahmed et al. (1984). Dimensions remain identical with length, width and height of $L=1044$ mm, $W=389$ mm and $H=288$ mm, respectively (Fig. 3). Unless otherwise specified, the rear slant was fixed at an angle of 25° from the horizontal for the present work, which corresponds to a wake dominated by large counter-rotating longitudinal vortices generated at the c-pillars (Ahmed et al., 1984). Only half of the body was simulated due to the symmetrical nature of the problem when observed through the time-mean state. The model was set at a height of 50 mm above a stationary ground board of length $3.68L$ and width $0.75L$ in the symmetry model, which extends $1.12L$ in front and $1.56L$ behind the body. The cylindrical stilts used to suspend the model for physical testing were omitted for simplicity.

To investigate the influence of longitudinal vortices on rear slant flow reattachment, the frontal aspect ratio of the Ahmed model was varied by widening or narrowing the body while the height remained fixed. It is proposed that varying the aspect ratio in this manner will influence the interaction between the c-pillar vortices and the flow over the rear slant. The definition of aspect ratio adopted in this paper is the ratio of the cross-sectional aspect ratio of the Ahmed model to the cross-sectional aspect ratio of the standard-dimension Ahmed model (Eq. (1)), and from hereon will be denoted simply as aspect ratio (AR). Since the height of the model is fixed for all cases, this effectively reduces to a ratio of model widths. Aspect ratios between 0.6 and 1.6 were simulated in increments of 0.1, with additional increments where increased resolution was required:

$$AspectRatio\ (AR) = \frac{AR_{model}}{AR_{standard}} = \frac{W_{model}}{W_{standard}} \tag{1}$$

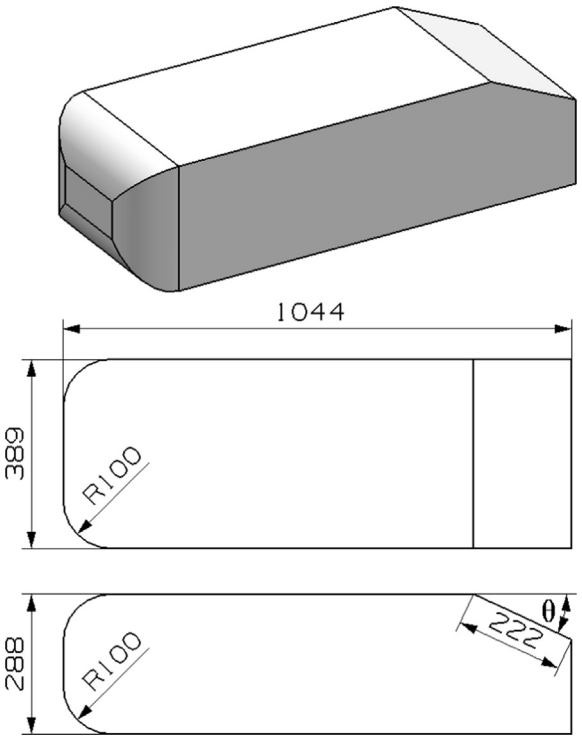

Fig. 3. Ahmed-body geometry (dimensions in mm).

The numerical model was based on a steady formulation of the RANS equations solved using the commercial CFD package STAR-CCM+ (version 6.04.014). Turbulence modelling was accomplished using the k–ω SST model proposed by Menter (1994), which is a hybrid model that blends between a k–ω formulation in the inner region of the boundary layer and a k–ϵ formulation in the outer region and areas of free shear flow. This model offers improved accuracy over the standard k–ϵ model in areas of adverse pressure gradient, and allows resolution of the boundary layer down to the wall. It also does not suffer from the problem of inlet freestream turbulence sensitivity associated with the standard k–ω model (Menter, 1994).

The computational domain has a total length of 15L (4L upstream and 10L downstream of the body), a width of 3L and a height of 3L, which equates to a numerical blockage of between 0.34% and 0.91% for the varying AR cases (Fig. 4). Through a domain independence study on the standard Ahmed model, it was shown that the blockage effects in a domain with a width and height of 1.5L and 3L respectively were negligible (Table 1). However, the domain width was conservatively increased to 3L to account for the increased spanwise blockage of the higher AR models to be tested. An inlet velocity of 1.47 m/s was imposed as the upstream boundary condition, corresponding to a Reynolds number based on model length of 9.8×10^4, as well as an inlet freestream turbulence intensity of 0.5%. The Reynolds number for the present work was chosen so that the predictions would be directly comparable with those from concurrent water channel experiments being performed in our research group (Venning et al., 2015) at an identical Reynolds number, which was chosen as it is the maximum Reynolds number attainable for the available model in the water channel being used. Importantly, results at a Reynolds number of this order were shown to agree well with those at $Re \sim \mathcal{O}(10^6)$ (Spohn and Gilliéron, 2002), which is the order of magnitude generally used for Ahmed model experimental studies. Symmetry boundary conditions were set for the upper, side and symmetry boundaries of the numerical wind tunnel, while the ground was modelled as a no-slip wall for the ground board and a free-slip wall for the remaining ground plane. The ground board dimensions and boundary conditions were chosen to best replicate the splitter plate arrangement of the aforementioned water channel experiment, which is of particular importance for matching upstream boundary layer growth. The downstream outlet was set to a pressure outlet boundary condition.

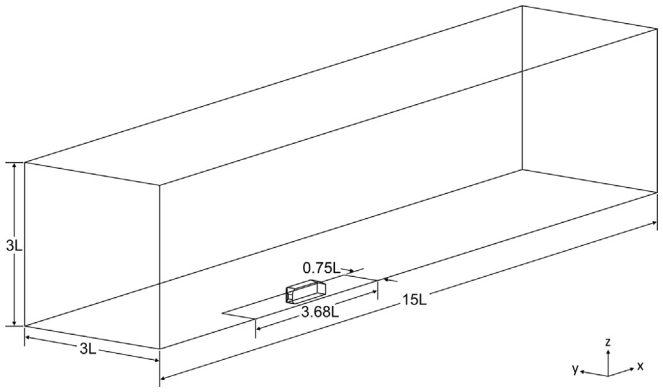

Fig. 4. The computational domain showing the key dimensions.

Table 1
Domain independence study of blockage effects.

Domain (width × height)	Blockage (%)	C_D	ΔC_D (%)
1.5L × 3L	1.14	0.324	–
3L × 6L	0.286	0.322	−0.780
4.5L × 9L	0.143	0.323	0.471

The mesh is constructed entirely from polyhedral unstructured elements, with two stages of mesh refinement in the vicinity of the body to capture detailed flow structures around the body and into the wake region (Fig. 5). A prism layer mesh on the surface of the body and ground board is sized to ensure that a $y^+ \lesssim 1$ is achieved for accurate modelling of the near-wall boundary layer. All remaining mesh sizing was determined through an extensive mesh resolution study, whereby mesh sizings for all surfaces and regions were progressively refined until convergence was achieved. The mesh refinement was considered adequate for a mesh resolution such that the drag coefficient was within 1 percent of that of the finest mesh (see Fig. 6 for the effect on the drag of the number of prism layers spanning the viscous and log layers at the boundary of the model). The dimensions of the inner and outer mesh refinement regions were scaled with model AR to maintain sufficient resolution in the vicinity of the model. The final element count varied from approximately 17–27 million depending on geometry. For individual cases, solution convergence was assessed through monitoring of the drag coefficient, with all simulations attaining a drag coefficient deviation of less than 0.5% over the final 1000 iterations.

3. Validation

An initial sweep of slant angles was simulated as a baseline comparison with the experimental results obtained by Ahmed

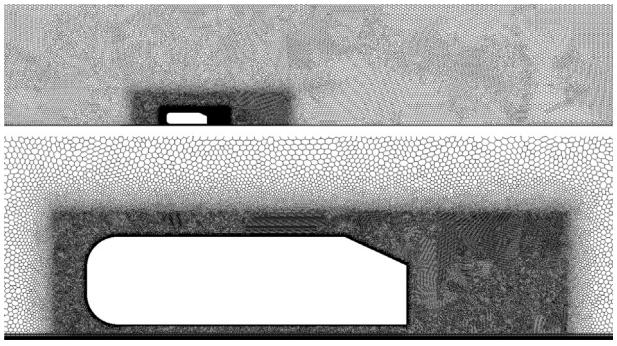

Fig. 5. Mesh distribution on the symmetry plane.

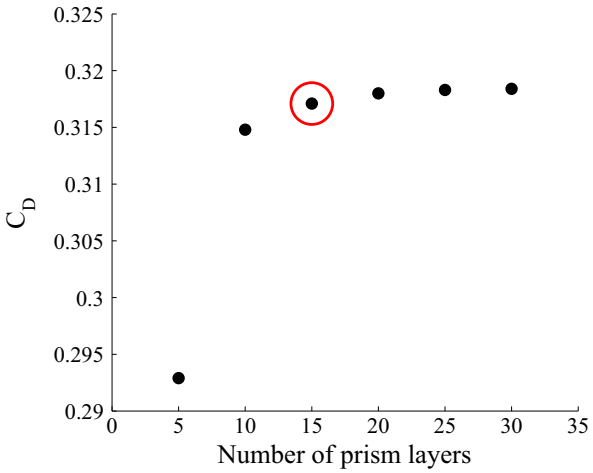

Fig. 6. Drag coefficient variation with boundary layer mesh refinement. The chosen number of layers is circled.

et al. (1984). This provided a means for validating the numerical model used, as well as for comparing the effect of the lower Reynolds number used for the present investigation.

Rear slant angles of between 0° and 30° were initially simulated in 5° increments, followed by local refinement in areas of interest. From Fig. 7, two main differences to the results obtained by Ahmed et al. (1984) can be observed. A shift in critical angle from 30° to 24° is evident, along with an upward shift in the values of drag coefficient for all angles other than the high-drag configuration at the 30° slant angle.

When the drag coefficient was decomposed into pressure drag components on the front, slant and base surfaces (Fig. 8), it was found that a majority of this shift in drag can be attributed to a relatively constant increase in pressure drag at the front surface of the body, across the entire slant angle range. Flow visualisation shows separation along the trailing edges of the corner radii joining the front to the roof and sides of the model, comparable to that observed in work by Spohn and Gilliéron (2002) in water channel testing at a Reynolds number of the same order of magnitude, as well as computational studies by Krajnović and Davidson (2005) and Minguez et al. (2008). This is in contrast to higher Reynolds number work on the Ahmed body, which was developed specifically for 'separation free flow over its (fore-body) surface' (Ahmed et al., 1984), and is a plausible explanation for the increase in drag coefficient experienced at the front of the model. The pressure drag on the slant surface matches closely with the experimental results of Ahmed et al. (1984) in both trend and magnitude, with the main difference resulting from the separation of the flow at a lower critical angle. Comparison of pressure drag at the base of the model shows a reducing discrepancy between results as slant angle increases.

The shift in the critical angle from the originally measured 30° to 24° is not well understood. Some studies of the Ahmed body have determined this critical angle to be 30° (Ahmed et al., 1984; Conan et al., 2011), though others only confine it to the range of between 25° and 35° (Brunn et al., 2007; Lienhart et al., 2002; Wang et al., 2013). However, it has also been shown that this critical angle is sensitive to both geometric and boundary constraints (such as mounting) (Strachan et al., 2007), as well as Reynolds number effects (Tunay et al., 2014). This is somewhat intuitive from the non-fixed nature of the reattachment point of the flow over the slant surface. Some Reynolds number dependence of the drag coefficient has also been demonstrated by Vino et al. (2005) for Reynolds numbers of the O(10^6), which could result from either changes in frontal separation or rear reattachment, or both. It is therefore plausible that the shift in critical angle is due to the lower Reynolds number of the present work when compared to the majority of experimental investigations of the Ahmed body (Ahmed et al., 1984; Brunn et al., 2007; Conan et al., 2011; Lienhart et al., 2002). It is also possible that the geometric differences, namely the omission of the stilts used for mounting the model in physical experiments, has influenced the critical slant angle to some extent. In any case, the discontinuity in the drag curve, which is associated with the global change in near-wake structure, is clearly resolved by the numerical model.

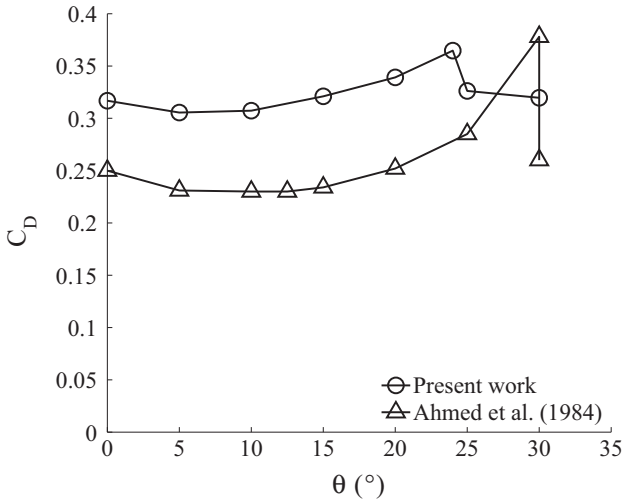

Fig. 7. Variation of predicted and measured drag coefficients with slant angle.

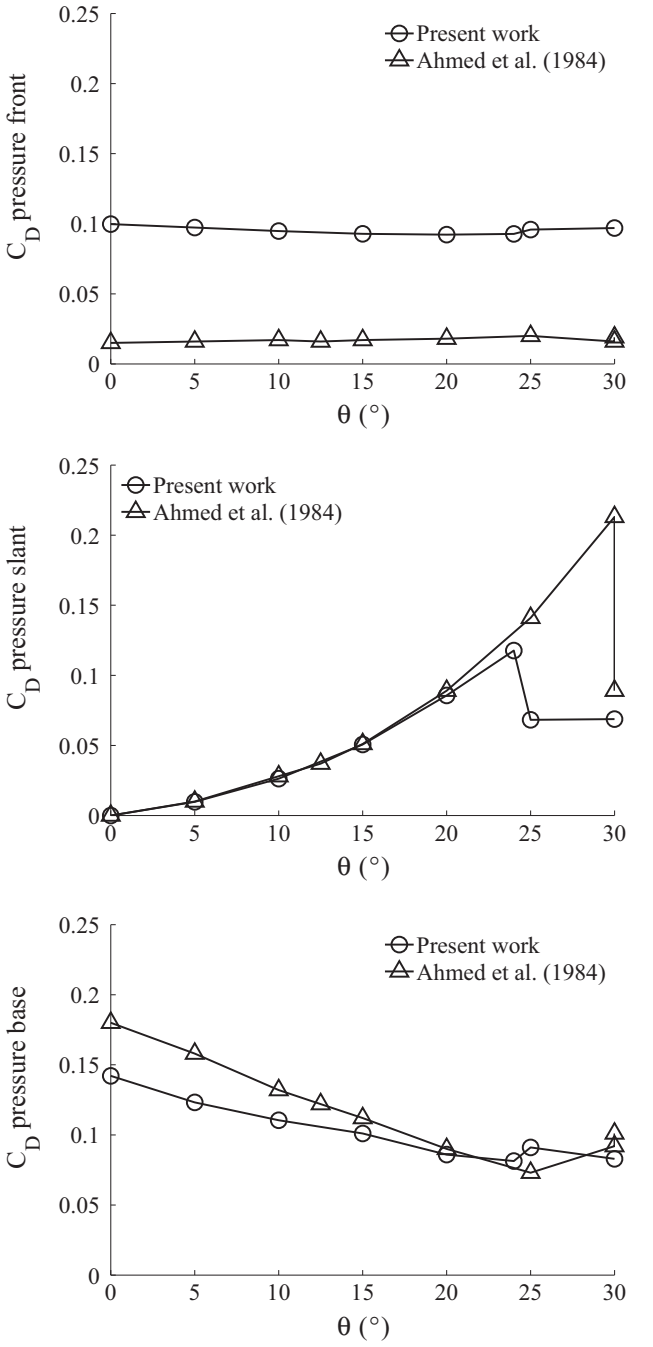

Fig. 8. Breakdown of pressure drag into contributions from front, slant and base of model.

4. Results

Frontal aspect ratios vary considerably between different hatchback models in the automotive industry, and therefore a better understanding of the effect of AR on flow attachment and wake structures is paramount to advances in aerodynamic design for this type of vehicle. Ahmed model ARs of between 0.6 and 1.6 were investigated, with slant angle held constant at 25° for these experiments.

4.1. Force and pressure measurements

Drag coefficient is shown in Fig. 9 to vary linearly with AR between the values simulated, with a discontinuous drop occurring between AR of 0.85 and 0.90. Similarly, the lift coefficient experiences a discontinuity within this range of AR. A breakdown of the pressure drag coefficient into its various components (Fig. 10) indicates that the rear slant is the main contributing surface to the discontinuous behaviour of the drag curve. A much smaller discontinuity exists in the pressure drag on the base surface, while the frontal surface experiences no apparent discontinuity.

The increase in drag coefficient with AR observed in the linear regions of Fig. 9 can be seen in Fig. 10 to be predominantly generated at the front surfaces of the model. Neglecting the discontinuity, the change in pressure drag at the base of the model is

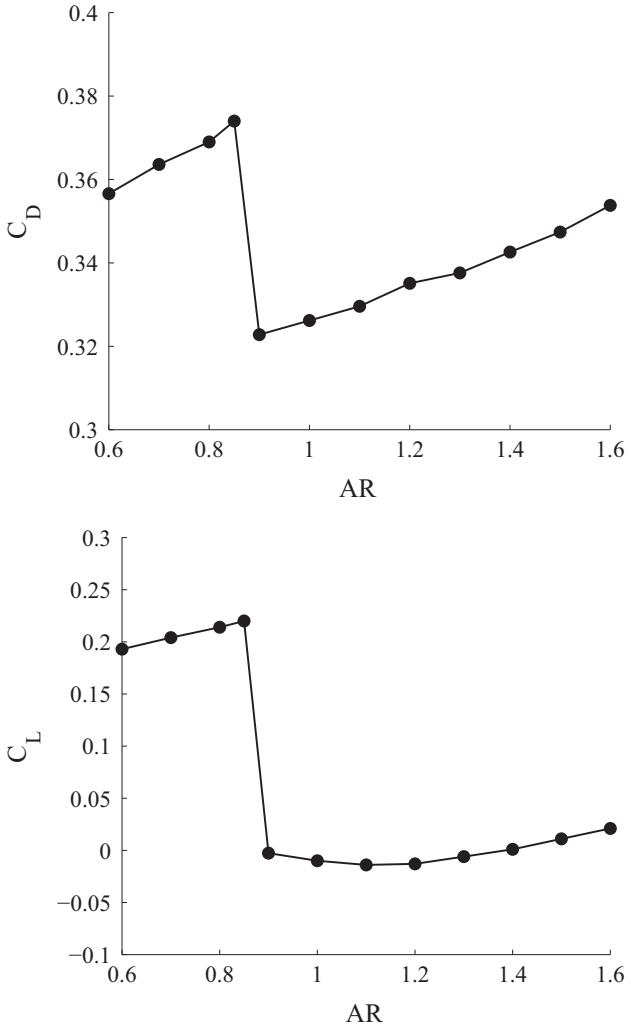

Fig. 9. Variation of drag and lift coefficients with aspect ratio.

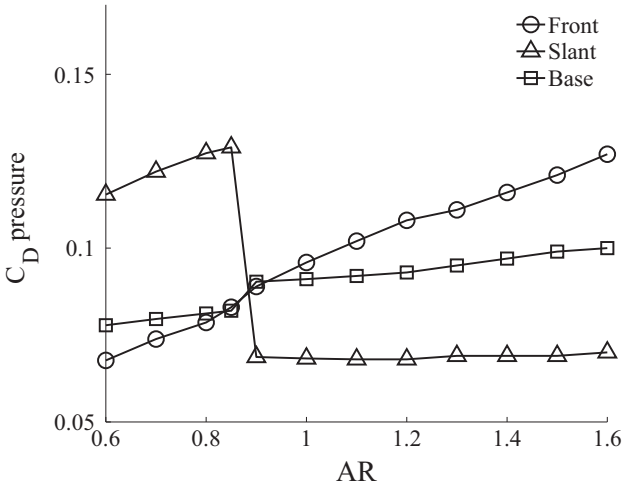

Fig. 10. Pressure drag components.

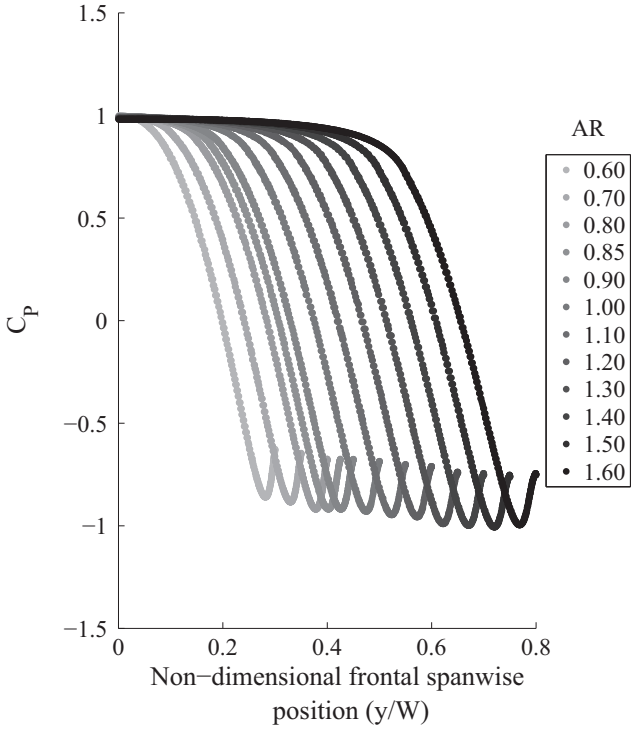

Fig. 11. Frontal spanwise pressure distribution at mid-height of model.

minimal across the AR range, while at the slant surface the change is negligible. Spanwise frontal pressure distribution at the mid-height of the model (Fig. 11) indicates that the additional drag generated at the front of the model with increasing AR is a direct result of a widening of the frontal high-pressure region. The flow around the edge radius varies only marginally with AR, with the suction peak increasing slightly as the body width increases.

4.2. Flow visualisation

Fig. 12 shows that between AR of 0.85 and 0.9, a change in the flow at the rear of the model occurs. At an AR of 0.85, the flow separates from the leading edge of the rear slant and appears to reattach onto the slant further downstream. The separation bubble is quite large, with the observed attached flow restricted to only a small portion of the slant. A closer inspection of the slant surface streamlines and vectors in Fig. 13 shows that flow reattachment

does not occur along the line of symmetry of the model, but rather it is restricted to the edges of what is a large recirculation bubble which dominates the flow over the slant. The slant surface flow resembles significantly the experimental flow visualisation by Spohn and Gilliéron (2002), with larger than usual recirculation bubble and lack of central flow reattachment likely being due to the close proximity of this particular case to the critical flow conditions. The c-pillar vortex is seen in Fig. 13 to emanate from the leading-edge corner of the slant and is progressively drawn inwards as it travels downstream. The low pressure regions generated by both the recirculation bubble and c-pillar vortex are observed to have a large effect on the slant surface pressure (Fig. 13).

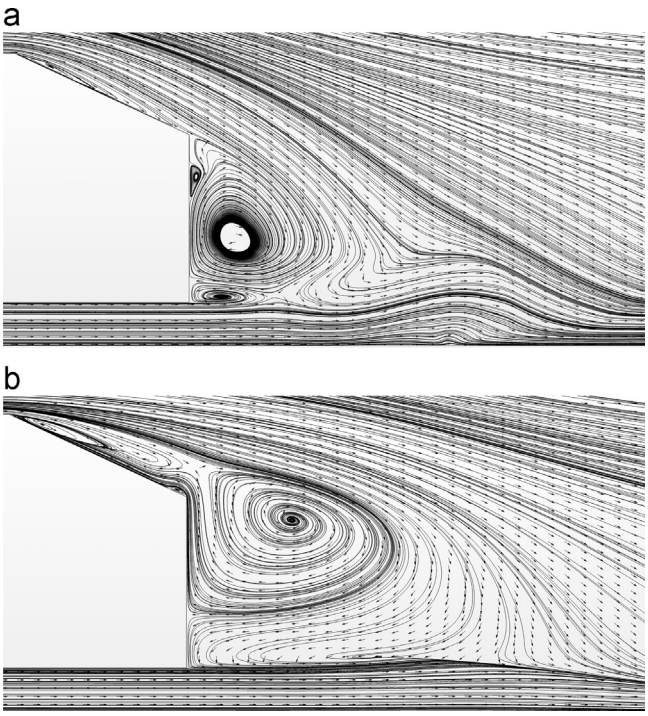

Fig. 12. Symmetry plane flow vectors and streamlines in wake. (a) AR=0.85 and (b) AR=0.90.

Fully separated flow occurs at AR of 0.9, and a significant increase in pressure results on the rear-slant surface (Figs. 12 and 13). Influence of the c-pillar vortex is not seen in either the surface flow topology or the surface pressure contours. A small recirculating zone caused by flow driven up from the base of the body is the cause of the reattachment line towards the trailing edge of the rear slant. It is also observed that the recirculating region in the wake of the body increases considerably in size between the two ARs in Fig. 12.

Rotationally dominated flow, visualised using an isosurface of the Q-criterion (Jeong and Hussain, 1995), demonstrates significant vortex activity initiating at various sites on the model (Fig. 14). Counter-rotating pairs of longitudinal vortices emanate near the front of the model on both the roof and sides from separation foci within the frontal separated regions (Spohn and Gilliéron, 2002). Also prominent in the flow are longitudinal vortices running alongside the bottom corner of the model, which are the result of vorticity generated from outwards moving flow between the underside and ground plane (Wang et al., 2013). These frontal and mid-section generated structures remain essentially identical across the drag discontinuity.

The characteristic longitudinal counter-rotating vortex pair develop along the c-pillars for both 0.85 and 0.90 AR cases, though qualitatively they appear to be substantially diminished in the latter case. Vortex structures generated by the rear slant recirculation bubble (Spohn and Gilliéron, 2002) are drawn downwards into the wake for the 0.85 AR case as a result of the flow being attached at the trailing edge of the slant.

The change in flow regime observed across the aspect ratios in Figs. 12–14 is identical to that described in Ahmed body literature across the critical slant angle (Ahmed et al., 1984; Conan et al., 2011; Lienhart et al., 2002; Wang et al., 2013). In addition, the discontinuity in drag force seen in Fig. 9 is what characteristically accompanies this change in flow regime. It is therefore intuitive that the change in model AR has had a direct influence on the critical slant angle of the model, whereby the widening of the model has resulted in the critical slant angle decreasing.

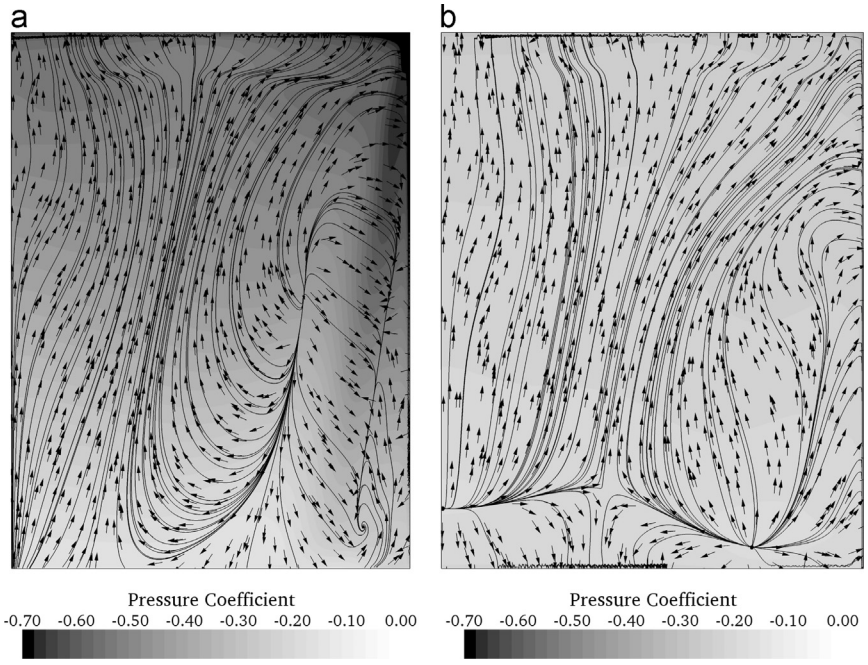

Fig. 13. Rear slant flow topology and surface pressure coefficient (Note: Left edge of slant surface is line of symmetry). (a) AR=0.85 and (b) AR=0.90.

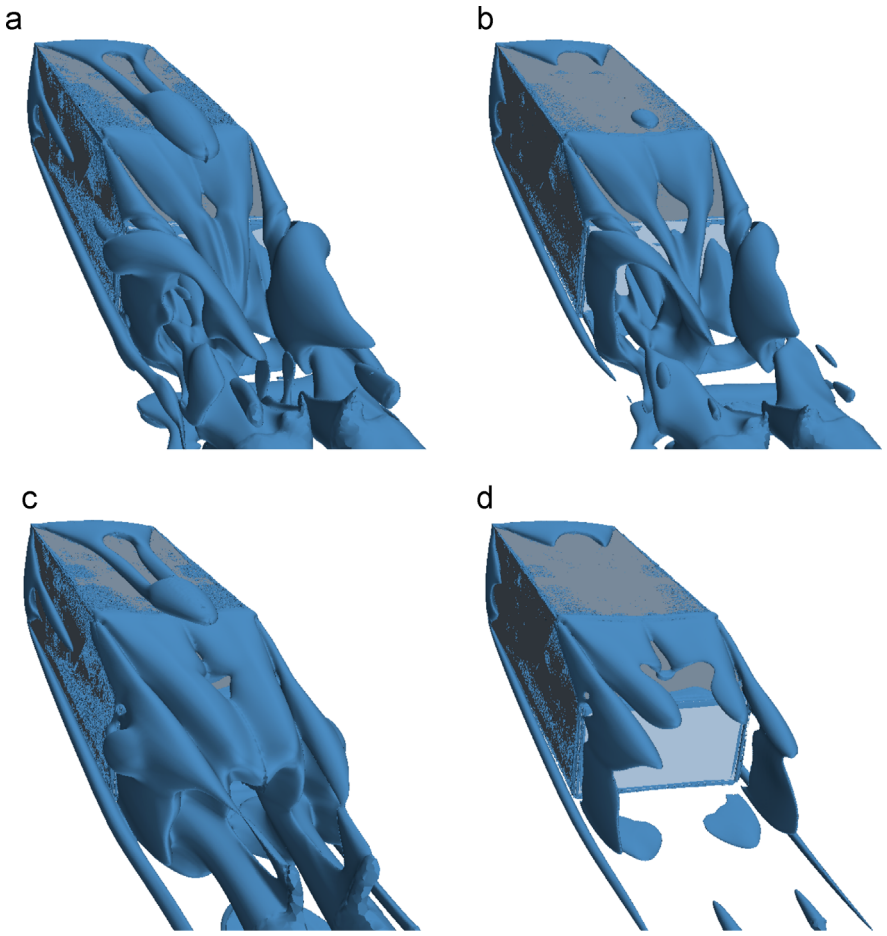

Fig. 14. Isosurfaces of Q-criterion for aspect ratios of 0.85 and 0.90. (a) AR=0.85, Q=5, (b) AR=0.85, Q=20, (c) AR=0.90, Q=5 and (d) AR=0.90, Q=20.

The most likely explanation for this is that the widening of the model changes the influence that c-pillar vortex downwash has on promoting the flow to reattach onto the model slant. As the model width increases, the recirculation bubble above the rear slant grows in width, and the c-pillar vortices shift further away from the centre of the bubble where reattachment is most critical. At the critical AR, the influence of the c-pillar vortex downwash on reattachment has been sufficiently diminished to cause fully separated rear slant flow to occur.

This result is comparable to that seen by Venning et al. (2015) in water channel testing on an Ahmed model with varying aspect ratio. Here it was found that the discontinuity occurred between ARs of 1.0 and 1.1, somewhat higher than the present results, which could be attributed to factors such as differences in model blockage and the omission of the model stilts used in the physical experiments. Qualitatively however, the results compare favourably, with both the transition from reattaching to fully separated flow as well as the significant reduction in c-pillar vortex strength being observed discontinuously with increasing model aspect ratio.

4.3. C-Pillar vortex behaviour

Vortex core position and bounds were determined using the Gamma 2 (Γ_2) criterion for vortex identification (Graftieaux et al., 2001). The Γ_2 criterion is a non-local, Galilean-invariant method which assigns values of Γ_2 in the flow field based purely on geometrical considerations of the velocity field topology:

$$\Gamma_2(P) = \frac{1}{N}\sum_{S}\frac{[\overrightarrow{PM} \wedge (\mathbf{U}_M - \tilde{\mathbf{U}}_P)] \cdot \mathbf{e}_z}{\| \overrightarrow{PM} \| \cdot \| \mathbf{U}_M - \tilde{\mathbf{U}}_P \|}. \quad (2)$$

Here, P is a fixed point in the measurement domain, S is a two-dimensional area surrounding P, M lies in S, $\mathbf{e}_z$ is the unit vector normal to the measurement plane, $\mathbf{U}_M$ is the velocity vector at M, and $\tilde{\mathbf{U}}_P = (1/S)\int_S \mathbf{U} \cdot d\mathbf{S}$ is the local convective velocity. Using this method, a vortex core is considered to be any point in the flow at which the value of Γ_2 exceeds $2/\pi$.

Across the change in flow regime observed between AR of 0.85 and 0.9, the c-pillar vortices experience an almost 70 percent reduction in strength, whilst also shifting upwards and therefore away from the surface of the rear slant (Fig. 15). The effect of this change on the rear slant surface pressure was discussed previously and is clearly evident in Fig. 13. Before and after the critical AR, c-pillar vortex strength varies only marginally, while its distance from the ground plane gradually increases with increasing AR. The reduction in c-pillar vortex strength that accompanies the flow regime change is also observed in the experiments of Venning et al. (2015).

It is of particular interest to note that while c-pillar vortices appear to play a critical role in promoting flow to reattach onto the rear slant of the Ahmed model, it is clearly evident in Fig. 15 that the reattaching flow regime provides a significant proportion of the mechanisms required for c-pillar vortex generation. Reattaching flow over the rear slant allows much more of the vorticity that is generated along the sides of the model to be skewed into

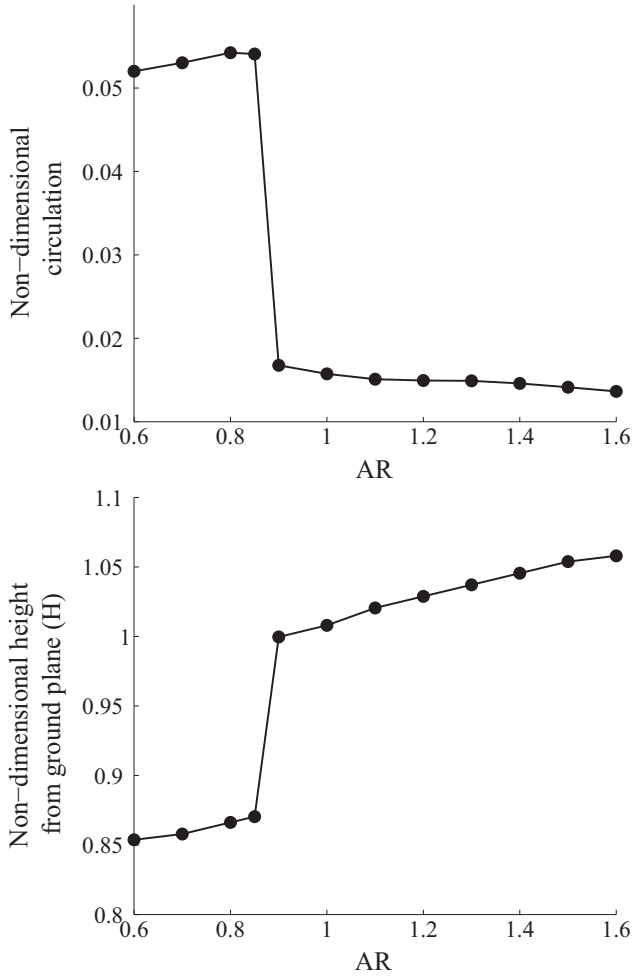

Fig. 15. C-pillar vortex strength and height from ground plane at $x/L = 0.1$ downstream of model.

the streamwise direction as it rolls over the c-pillars of the model, resulting in significantly stronger c-pillar vortex structures.

5. Conclusions

The effect of slant angle on drag force and wake structures has been the subject of many past investigations into the Ahmed model. As a result, the characteristic drag curve including the drag discontinuity and the wake flow of this simplified automotive model are reasonably well understood. However, the significance of aspect ratio on the model and its effect on the characteristic drag curve and critical slant angle is a notable omission from any investigations thus far. This is surprising considering the vast array of vehicle aspect ratios existent in the automotive industry, and the severe implications that slant angle choice coupled with aspect ratio can have on overall vehicle drag characteristics.

This study has found that the critical slant angle does vary with model aspect ratio, which results from the interaction that the longitudinal c-pillar vortices have with the flow over the rear slant. As the c-pillar vortices are moved further apart, the influence that their downwash has on promoting flow reattachment diminishes. This is evident by the discontinuous drag curve observed for varying aspect ratio where, between aspect ratios of 0.85 and 0.90, the increase of the c-pillar vortex spacing causes unsustainable flow reattachment and fully separated flow occurs. It can also be remarked that whilst it is the influence of the c-pillar vortices that to some extent promote the flow to reattach onto the rear slant surface of the model, it is also evident that the reattaching flow and low-pressure recirculation bubble are what retain the c-pillar vortices close to the slant surface and also provide mechanisms for vorticity generated along the model to be skewed into the streamwise direction. There is therefore a mutually dependent relationship between these two main flow structures.

The Reynolds number of the flow in this study is significantly lower than that which would be experienced in general automotive use, and a plausible case for Reynolds number dependence of both the flow over the front and the rear of the model was made. However, while predicted drag values for this study may not be precisely applicable to high Reynolds number automotive flows, the essentially identical wake flow structures observed for reattaching and fully separated flow cases provide reasonable justification for expecting similar aspect ratio effects at higher Reynolds numbers.

Acknowledgements

This research was undertaken with the assistance of resources provided at the NCI National Facility systems at the Australian National University through the National Computational Merit Allocation Scheme (Project d71) supported by the Australian Government. The authors acknowledge financial support for the project through the Australian Research Council (ARC) Linkage Project Grant LP0991170.

References

Ahmed, S.R., Ramm, G., Faltin, G., 1984. Some salient features of the time-averaged ground vehicle wake. SAE Technical Paper 840300.
Baker, C.J., 2010. The flow around high speed trains. J. Wind Eng. Ind. Aerodyn. 98, 277–298.
Brunn, A., Wassen, E., Sperber, D., Nitsche, W., Thiele, F., 2007. Active drag control for a generic car model. In: King, R. (Ed.), Active Flow Control, vol. 95. Springer, Berlin, Heidelberg, pp. 247–259.
Conan, B., Anthoine, J., Planquart, P., 2011. Experimental aerodynamic study of a car-type bluff body. Exp. Fluids 50, 1273–1284.
Gerich, D., Eckelmann, H., 1982. Influence of end plates and free ends on the shedding frequency of circular cylinders. J. Fluid Mech. 122, 109–121.
Gilhome, B.R., Saunders, J.W., Sheridan, J., 2001. Time averaged and unsteady near-wake analysis of cars. SAE Technical Paper 2001-01-1040.
Good, G.L., Garry, K., 2004. On the use of reference models in automotive aerodynamics. SAE Tehcnical Paper 2004-01-1308.
Graftieaux, L., Michard, M., Grosjean, N., 2001. Combining piv, pod and vortex identification algorithms for the study of unsteady turbulent swirling flows. Meas. Sci. Technol. 12 (9), 1422–1429.
Hucho, W.-H., Sovran, G., 1993. Aerodynamics of road vehicles. Ann. Rev. Fluid Mech. 25, 485–537.
Janssen, L.J., Hucho, W.-H., 1975. Aerodynamische formoptimierung von vw golf und vw scirocco. Automob. Z. 77.
Jeong, J., Hussain, F., 1995. On the identification of a vortex. J. Fluid Mech. 285, 69–94.
Krajnović, S., Davidson, L., 2005. Flow around a simplified car, part 2: understanding the flow. J. Fluids Eng. 127 (September).
Lienhart, H., Stoots, C., Becker, S., 2002. Flow and turbulent structures in the wake of a simplified car model (Ahmed model). In: Notes on Numerical Fluid Mechanics, vol. 77. Springer, pp. 323–330.
Menter, F.R., 1994. Two-equation Eddy-viscosity turbulence models for engineering applications. AIAA J. 32 (August (8)), 1598–1605.
Minguez, M., Pasquetti, R., Serre, E., 2008. High-order large-Eddy simulation of flow over the Ahmed body car model. Phys. Fluids 20.
Morel, T., 1978. Aerodynamic drag of bluff body shapes characteristic of hatch-back cars. SAE Technical Paper 780267.
Noca, F., Shields, D., Jeon, D., 1999. A comparison of methods for evaluating time-dependent fluid dynamic forces on bodies, using only velocity fields and their derivatives. J. Fluids Struct. 13, 551–578.
Okajima, A., Ueno, H., Sakai, H., 1992. Numerical simulation of laminar and turbulent flows around rectangular cylinders. Int. J. Numer. Methods Fluids 15, 999–1012.

Onorato, M., Costelli, A.F., Garrone, A., 1984. Drag measurement through wake analysis. SAE Technical Paper 840302.
Payne, F., Ng, T., Nelson, R., Schiff, L., 1986. Visualization and flow surveys of the leading edge vortex structure on delta wing planforms. AIAA Paper 86-0330.
Roshko, A., 1954. On the drag and shedding frequency of two-dimensional bluff bodies. NASA Technical Note 3169.
Spohn, A., Gilliéron, P., 2002. Flow separations generated by a simplified geometry of an automotive vehicle. In: IU-TAM Symposium: Unsteady Separated Flows, April 8–12.
Strachan, R.K., Knowles, K., Lawson, N.J., 2007. The vortex structure behind an Ahmed reference model in the presence of a moving ground plane. Exp. Fluids 42, 659–669.
Tan, B.T., Thompson, M.C., Hourigan, K., 2005. Evaluating fluid forces on bluff bodies using partial velocity data. J. Fluids Struct. 20 (1), 5–24.
Tunay, T., Sahin, B., Ozbolat, V., 2014. Effects of rear slant angles of the flow characteristics of Ahmed body. Exp. Therm. Fluid Sci. 57, 165–176.
Venning, J., Lo Jacono, D., Burton, D., Thompson, M., Sheridan, J., 2015. The effect of aspect ratio on the wake of the Ahmed body. Exp. Fluids 56.
Vino, G., Watkins, S., Mousley, P., Watmuff, J., Prasad, S., 2005. Flow structures in the near-wake of the Ahmed model. J. Fluids Struct. 20, 673–695.
Wang, X.W., Zhou, Y., Pin, Y.F., Chan, T.L., 2013. Turbulent near wake of an Ahmed vehicle model. Exp. Fluids 54.
Williamson, C.H.K., 1996. Vortex dynamics in the cylinder wake. Ann. Rev. Fluid Mech. 28, 477–539.